Titre: Title:	Quantitative pulsatility measurements using 3D dynamic ultrasound localization microscopy
Auteurs: Authors:	Chloé Bourquin, Jonathan Porée, Brice Rauby, Vincent Gaël Perrot, Nin Ghigo, Hatim Belgharbi, Samuel Bélanger, Gerardo Ramos-Palacios, Nelson Cortes, Hugo Ladret, Lamyae Ikan, Christian Casanova, Frédéric Lesage, & Jean Provost
Date:	2024
Type:	Article de revue / Article
Référence: Citation:	Bourquin, C., Porée, J., Rauby, B., Perrot, V. G., Ghigo, N., Belgharbi, H., Bélanger, S., Ramos-Palacios, G., Cortes, N., Ladret, H., Ikan, L., Casanova, C., Lesage, F., & Provost, J. (2024). Quantitative pulsatility measurements using 3D dynamic ultrasound localization microscopy. Physics in Medicine and Biology, 69(4), 045017 (14 pages). https://doi.org/10.1088/1361-6560/ad1b68

Document en libre accès dans PolyPublie
Open Access document in PolyPublie

URL de PolyPublie: PolyPublie URL:	https://publications.polymtl.ca/57387/
Version:	Version officielle de l'éditeur / Published version Révisé par les pairs / Refereed
Conditions d'utilisation: Terms of Use:	CC BY

Document publié chez l'éditeur officiel
Document issued by the official publisher

Titre de la revue: Journal Title:	Physics in Medicine and Biology (vol. 69, no. 4)
Maison d'édition: Publisher:	IOP Publishing Ltd
URL officiel: Official URL:	https://doi.org/10.1088/1361-6560/ad1b68
Mention légale: Legal notice:	

PAPER • OPEN ACCESS

Quantitative pulsatility measurements using 3D dynamic ultrasound localization microscopy

To cite this article: Chloé Bourquin *et al* 2024 *Phys. Med. Biol.* **69** 045017

View the article online for updates and enhancements.

Physics in Medicine & Biology

IPEM
Institute of Physics and
Engineering in Medicine

CrossMark

PAPER

Quantitative pulsatility measurements using 3D dynamic ultrasound localization microscopy

Chloé Bourquin[1] , Jonathan Porée[1] , Brice Rauby[1] , Vincent Perrot[1] , Nin Ghigo[1] ,
Hatim Belgharbi[1,2] , Samuel Bélanger[3] , Gerardo Ramos-Palacios[4] , Nelson Cortes[5] , Hugo Ladret[5,6] ,
Lamyae Ikan[5] , Christian Casanova[5] , Frédéric Lesage[7,8] and Jean Provost[1,8]

1 Department of Engineering Physics, Polytechnique Montréal, Montréal, QC H3T 1J4, Canada
2 Department of Biomedical Engineering, University of North Carolina, Chapel Hill, NC 27599, United States of America
3 Labeo Technologies Inc., Montréal, QC H3V 1A2, Canada
4 Montreal Neurological Institute, McGill University, Montréal, QC H3A 2B4, Canada
5 School of Optometry, University of Montreal, Montréal, QC H3T 1P1, Canada
6 Institut de Neurosciences de la Timone, UMR 7289, CNRS and Aix-Marseille Université, Marseille, F-13005, France
7 Department of Electrical Engineering, Polytechnique Montréal, Montréal, QC H3T 1J4, Canada
8 Montreal Heart Institute, Montréal, QC H1T 1C8, Canada

E-mail: jean.provost@polymtl.ca

Abstract

A rise in blood flow velocity variations (i.e. pulsatility) in the brain, caused by the stiffening of
upstream arteries, is associated with cognitive impairment and neurodegenerative diseases. The study
of this phenomenon requires brain-wide pulsatility measurements, with large penetration depth and
high spatiotemporal resolution. The development of dynamic ultrasound localization microscopy
(DULM), based on ULM, has enabled pulsatility measurements in the rodent brain in 2D. However,
2D imaging accesses only one slice of the brain and measures only 2D-projected and hence biased
velocities . Herein, we present 3D DULM: using a single ultrasound scanner at high frame rate
(1000–2000 Hz), this method can produce dynamic maps of microbubbles flowing in the bloodstream
and extract quantitative pulsatility measurements in the cat brain with craniotomy and in the mouse
brain through the skull, showing a wide range of flow hemodynamics in both large and small vessels.
We highlighted a decrease in pulsatility along the vascular tree in the cat brain, which could be mapped
with ultrasound down to a few tens of micrometers for the first time. We also performed an intra-
animal validation of the method by showing consistent measurements between the two sides of the
Willis circle in the mouse brain. Our study provides the first step towards a new biomarker that would
allow the detection of dynamic abnormalities in microvessels in the brain, which could be linked to
early signs of neurodegenerative diseases.

1. Introduction

Arterial stiffening and the subsequent rise in pulsatility in downstream microvessels is known to be associated
with neurodegenerative diseases such as Alzheimer's disease (AD) (van den Kerkhof *et al* 2023). AD patients were
not only found to have a higher pulsatility index (PI) (Gosling and King 1974) in cerebral arteries compared to
controls (Roher *et al* 2011), but a high pulsatility in non-demented subjects was also linked to a significant
cognitive decline a few years later (Chung *et al* 2017). These findings suggests that a high pulsatility might be
involved in the early pathogenesis of some neurodegenerative diseases.

Thus, assessing the blood flow pulsatility in main cerebral arteries with transcranial Doppler (TCD)
ultrasound was proposed as a tool to monitor the progression of neurodegenerative diseases such as AD (Tomek
et al 2014). However, even at high frequency (Xu *et al* 2008), TCD only allows for pulsatility measurements in

major vessels, which may not be sufficient to report on pulse transmission to downstream microvessels and potential damage. Other brain imaging techniques such as optical coherence tomography (Baraghis *et al* 2011) or two-photon microscopy (Santisakultarm *et al* 2012) can also perform pulsatility measurements in microvessels at the surface of the brain, but do not provide sufficient penetration depth to achieve brain-wide pulsatility measurements.

A new imaging technique was recently developed, called ultrasound localization microscopy (ULM), or sometimes super-resolution ultrasound imaging (Couture *et al* 2011, Couture *et al* 2018, Christensen-Jeffries *et al* 2020). It consists in injecting microbubbles in the blood stream to follow them in the vascular tree using an ultrasound system. After a few minutes of acquisition, isolated microbubbles are localized with a subwavelength precision and tracked across frames to produce a map of the vasculature with a resolution of approximately 10 μm. ULM was applied in 2D in small animals (Christensen-Jeffries *et al* 2015, Errico *et al* 2015, Foiret *et al* 2017) and later in humans to perform angiographies of the brain, kidney, liver and heart (Demené *et al* 2021, Huang *et al* 2021, Denis *et al* 2023, Yan *et al* 2023). More recently, 3D ULM was demonstrated in small animals in several organs or tissues, including the rodent kidney (Taghavi *et al* 2022) brain (Heiles *et al* 2019, Chavignon *et al* 2022a, Demeulenaere *et al* 2022a, McCall *et al* 2023), and heart (Demeulenaere *et al* 2022b). In brain studies in particular, 2D ULM was shown to retrieve blood flow parameters such as cerebral vascularity, mean blood velocity and vessel tortuosity in an Alzheimer's mouse model (Lowerison *et al* 2022), and systolic and diastolic velocities in the human brain (Demené *et al* 2021). The method was also tested to characterize strokes in the rodent brain, in both 2D (Hingot *et al* 2020) and 3D (Chavignon *et al* 2022b). In silico, it was shown that microbubble tracks in ULM could even contain more information such as the pulsatility (Wiersma *et al* 2022).

In particular, dynamic ultrasound localization microscopy (DULM) (Bourquin *et al* 2021) localizes microbubbles both in space and time within a periodic phenomenon (e.g. heart cycle, or repeated stimuli). The main difference between ULM and DULM is DULM's temporal resolution: after the acquisition, the sequence triggering of DULM allows us to know perform a retrospective analysis of the images to retrieve the position of each frame within the cardiac cycle, leading to a measurement of the velocity variations with a temporal resolution of a few milliseconds. Using DULM, brain-wide pulsatility measurements in microvessels in 2D were shown to be possible *in vivo*, in a rat brain with craniotomy and a mouse brain through skull and skin (Bourquin *et al* 2021), along with the detection of functional activation in a rat brain (Renaudin *et al* 2022). DULM was also used in the rat heart (Cormier *et al* 2021), where it successfully retrieved a pulsatility signal in the microbubbles density variations throughout the cardiac cycles.

Herein, we show that 3D DULM can produce highly resolved dynamic maps of microbubbles flowing in the vasculature at a high frame rate using a single ultrasound scanner, and perform quantitative pulsatility measurements in the cat brain with craniotomy and in the mouse brain through the skull. In the cat brain, we showed a significant pulsatility attenuation in the vascular tree, from large feeding vessels to downstream smaller ones. An intra-animal validation of the measurements was performed in the mouse brain using the symmetry of the Willis circle. This novel method could be used to better understand blood flow dynamics in the vascular tree, by performing deep pulsatility measurements in the brain.

2. Methods

2.1. *In vivo* experiments

2.1.1. Ethics
All surgical and experimental procedures were undertaken according to the guidelines of the Canadian Council on Animal Care and were approved by the Ethics Committee of the University of Montreal (CDEA 19–008 and 19–064).

2.1.2. Animals' preparation
<u>Cat</u>: detailed procedures are described in Cortes *et al* (2022). Before surgery, a 3.64 kg female cat received a solution of atropine (0.1 mg kg^{-1}) and acepromazine (Atravet, 1 mg kg^{-1}) subcutaneously. Anesthesia was induced with 3.5% isoflurane in a 50:50 gas mixture of O$_2$ and N$_2$O. A catheter was placed in the cephalic vein to provide intravenous access. A tracheotomy was performed, which is recommended when using urethane (Moldestad *et al* 2009), before transfering the animal to the stereotaxic apparatus. Following anesthetic induction, isoflurane concentration was 1.5% during surgical procedures. During recording sessions, to avoid the vasodilation effects of isoflurane, the anesthesia was changed to halothane (0.5%–0.8%) in a 30:70 gas mixture of O$_2$ and N$_2$O. An intravenous bolus injection of 2% gallamine triethiodide was administered through the cephalic vein to induce muscular paralysis, and subsequently, the animal was placed under artificial ventilation. A 1:1 solution of 2% gallamine triethiodide (10 mg kg^{-1} h^{-1}) in 5% of dextrose in lactated Ringer's solution was continuously administered intravenously. Expired levels of CO$_2$ were maintained between 35 and

Table 1. 3D ultrasound imaging sequence gated on the ECG.

Sequence parameters	Cat brain	Mouse brain
Probe		2D matrix probe
Bandwidth		60%
Active elements		1024 (32 × 32)
Pitch (mm)		0.3
Center frequency (MHz)		7.81
Transmitted frequency (MHz)		6
Sampling		100%
Duty cycle		67%
Voltage (V)		30
# of groups acquired		800
# of transmits/receives		4 per frame at angle 0°
Mechanical index	0.09	0.09
# of cycles	4	2
Frame rate (Hz)	1000	2000
Penetration depth (mm)	37	19
# of frames acquired per group	600	400
Heart rate (bpm)	160	504
# of cardiac cycles per group	1.6	1.7
Total acquisition time (min)	15	17
Effective acquisition time (min)	8	3

40 mmHg by adjusting the tidal volume and respiratory rate. Temperature, SpO_2 and heart rate were monitored during the whole experiment. 3D *in vivo* DULM imaging of the cat brain was performed after a three-day optical imaging experiment, during which the animal was immobilized and under anesthesia (data not shown for the current study). Just before the ultrasound imaging, a 15×15 mm^2 craniotomy window was performed on the contralateral side of the one used for optical imaging procedures, in order to mitigate any potential harm to the associated tissue, despite the absence of any discernibly injury. A durotomy was performed to limit the aberrations due to the skull, and ultrasound gel was applied on the brain surface. The animal's heart rate was monitored throughout the procedure (Labeo Technologies Inc., QC, Canada). A 2 ml solution of 1 ml of microbubbles (1.2×10^{10} microbubbles per milliliter, Definity, Lantheus Medical Imaging, MA, USA) diluted in 1 ml of saline was injected as a bolus in the paw using a catheter. To minimize any potential complication, the catheter was placed in the animal's paw opposite to the one used for the gallamine and lactated Ringer's solutions administration.

Mouse: After sedation with chlorprothixene (5 mg kg^{-1}), a 16 week old female mouse weighting 24 g was anesthetized with urethane (1.0–1.5 g kg^{-1}, i.p., at 10% w/v in saline). Atropine (0.05 mg kg^{-1}) was also injected to reduce secretions in the airway. A tracheotomy was performed, which is recommended when using urethane (Moldestad *et al* 2009). The animal was placed on a platform (Labeo Technologies Inc., QC, Canada), where temperature and heart rate were monitored throughout the experiment. Before exposing the skull, a subcutaneous injection of lidocaine 2% was applied. The skin above the skull was removed, to ensure that the images would not be degraded by unshaved hair or air bubbles on the skin. Then, ultrasound gel was applied on the skull surface. A 50 μl solution containing 25 μl of microbubbles in solution (1.2×10^{10} microbubbles per milliliter, Definity, Lantheus Medical Imaging, MA, USA) and 25 μl of saline was injected as a bolus in the tail vein.

2.1.3. Ultrasound acquisitions

3D *in vivo* ultrasound imaging of both species (see table 1) was performed using an 2D matrix probe centered at 7.81 MHz with a 60% bandwidth (Verasonics, WA, USA). This probe is a 32-by-35 matrix array, but the 9th, 17th and 25th lines were not connected, resulting in a total number of active elements equal to 1024 (32 × 32 elements). Since it has a 0.3 mm pitch, the transmitted frequency was lowered down to 6 MHz. Indeed, to avoid grating lobes completely, a pitch of less than one wavelength is needed when imaging in front of the probe (Stutzman and Thiele 2012), which is not possible with the matrix array used in this study, we thus used a lower center frequency to limit their effect. Indeed, a 6 MHz frequency corresponds to a normalized pitch of approximately 1.2λ, whereas a 7.8 MHz frequency corresponds to a normalized pitch of 1.5λ. The pulse length was set to 2 cycles for the mouse and 4 cycles for the cat, to maintain a good contrast in the cat's brain despite a large imaging depth. The probe was placed at the surface of the mouse's skull (resp. the cat's brain) and connected to a programmable ultrafast ultrasound system (Vantage 256, Verasonics, WA, USA). As it is described in (Chavignon *et al* 2022a), driving a 2D-matrix array with a single ultrasound scanner requires to

adopt a multiplexing approach. In our sequence, each frame was completed with a succession of four Transmits/Receives: for one Transmit/Receive, we sent plane waves at angle 0° with all 1024 elements of the probe and received them with a sub-aperture of 256 elements (¼ of the probe). We primarily designed this sequence to image the cat brain and keep a high frame rate (1000 Hz) despite a high penetration depth (37 mm). The sequence was then adapted for the mouse brain, in which the 19 mm depth allowed for a frame rate of 2000 Hz.

Both animals were imaged using an ultrasound sequence synchronized with the ECG. In the cat brain, frames were acquired in groups of 600 during 15 min, in the mouse brain, frames were acquired in groups of 400 during 17 min. The sequence included pauses for data transfer and saving between each group. Without taking the pauses into account, the effective acquisition time was about 3 min for the mouse brain and 8 min for the cat brain. The first frame of each group started when the monitoring platform (Labeo Technologies Inc., QC, Canada) detected an R-wave in the ECG. Such a gated sequence allowed us to record almost two cardiac cycles for each group (1.6 cardiac cycles in the cat and 1.7 cardiac cycles in the mouse).

2.2. Data processing

2.2.1. DULM processing

As in Bourquin *et al* (2021), after a Delay-and-Sum (DAS) beamforming (Perrot *et al* 2021) on a $\lambda/2$ isotropic grid for the cat (resp. $\lambda/3$ for the mouse, to limit the grid-based artifacts that can appear after the microbubbles localization), the noise was normalized by dividing each pixel by the square root of the number of channels contributing to each pixel (Berthon *et al* 2018). We then used a singular value decomposition (SVD) filter on each group (600 frames for the cat and 400 frames for the mouse), to remove tissue by setting the first 20 singular values to zero. To enhance the microbubbles' signal, the images were correlated with the point spread function (PSF) of the system, which was simulated using an in-house GPU implementation of the SIMUS simulation software (Shahriari and Garcia 2018). The microbubbles were localized using a Gaussian least square fitting (Guo 2011), as a 1D fit in each direction (x, y, z). 1024 local maxima were detected in each frame, and only the ones with a high correlation coefficient (>0.2 in the mouse brain and >0.4 in the cat brain, chosen empirically to keep a sufficient number of microbubbles while limiting false detections) were kept as microbubbles for the following tracking algorithm. All these pre-processing algorithms (beamforming, tissue cancellation and localization, see figure 1) were implemented on MATLAB 2021a (The MathWorks, Inc., Natick, MA).

A linear Kalman filter was then used to track the microbubbles. We implemented an algorithm based on the one described in Tang *et al* (2020) and adapted it to 3D on Python 3.9, using a constant velocity model. For each new microbubble, we allocated a new Kalman filter to predict its position and velocity in the next frame. The prediction was then updated in the following frames, depending on the previous positions and velocities. As mentioned in Tang *et al* (2020), sparse microbubble positions were interpolated between frames along each track using an adaptive interpolation: the interpolation factor was set to obtain, in each track, a maximum distance between two consecutive microbubbles of $\sim 2~\mu$m in the mouse brain, and $\sim 5~\mu$m in the cat brain. This approach enabled the recovery of microbubbles positions, even in vessels where only a few microbubbles were detected, and to follow microbubbles with different behaviors (fast, slow, accelerating, etc) from one frame to another, to finally calculate their velocity. No other constraint, e.g. on the microbubbles' trajectory or acceleration, were used.
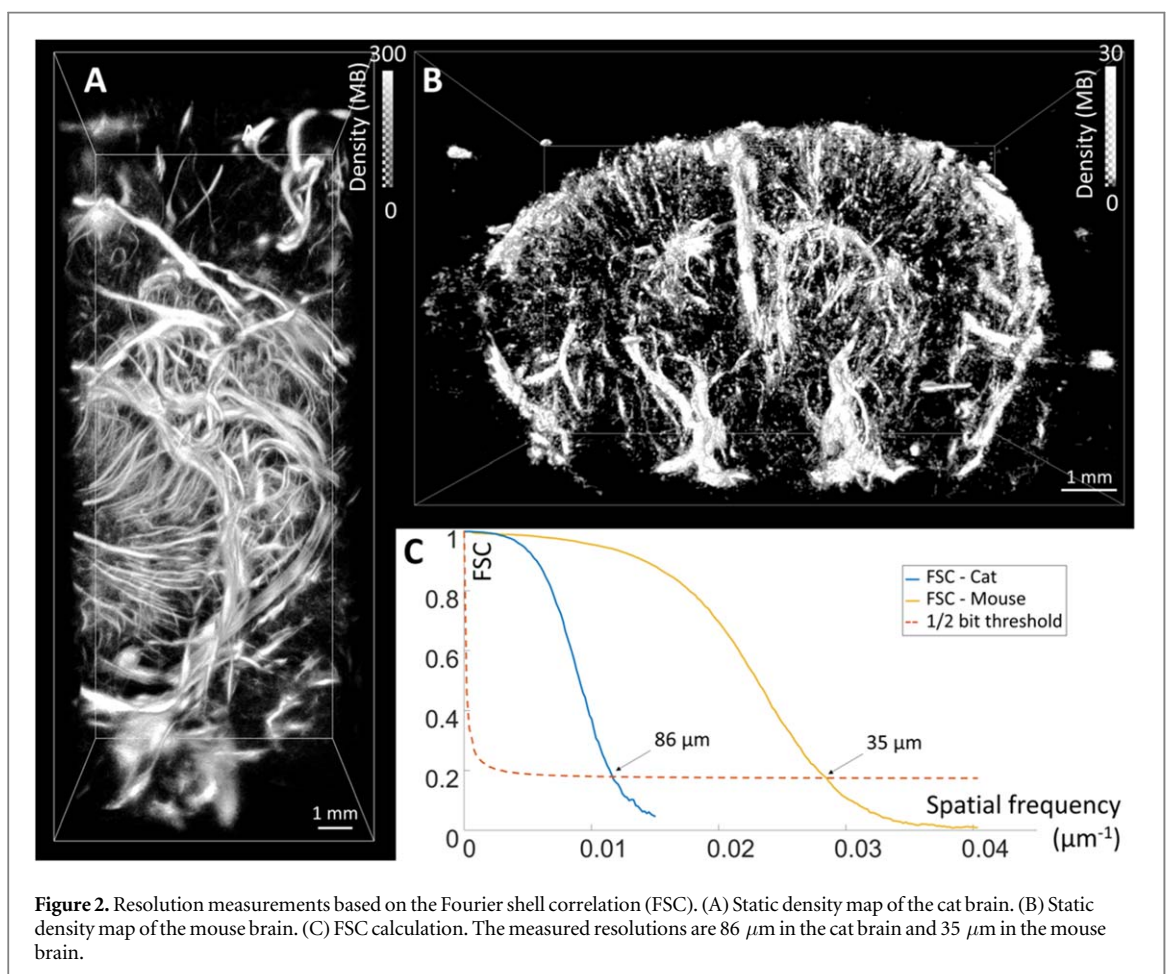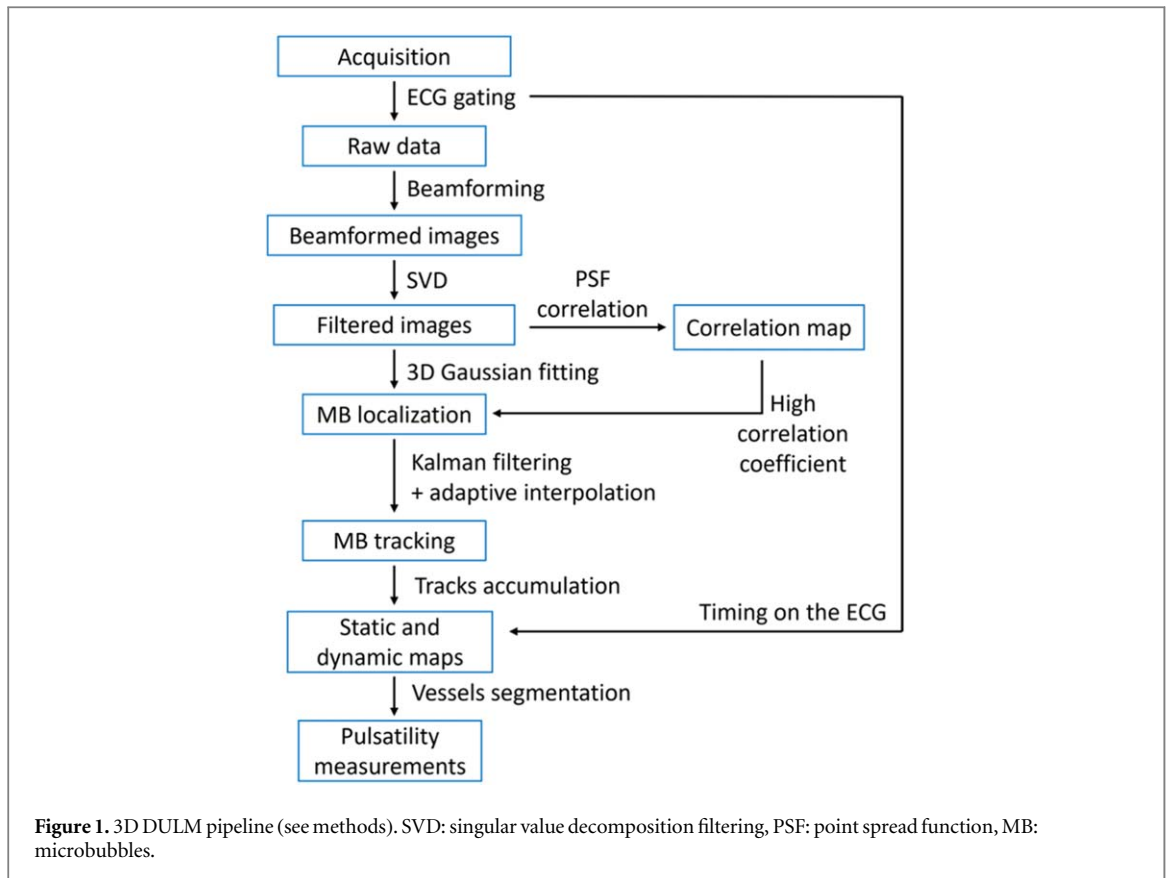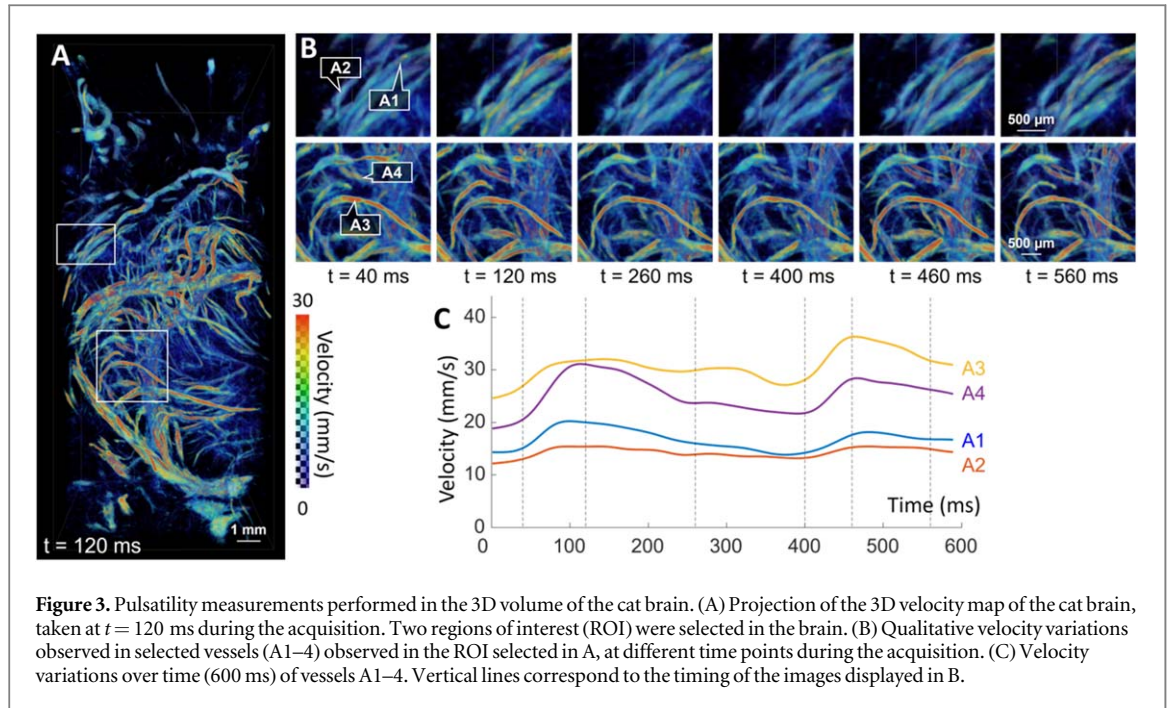
2.2.2. Dynamic maps

As described in Bourquin *et al* (2021), after tracking, the microbubbles' positions and velocities were averaged across all the groups according to their timing in each ECG-gated acquisition. By doing so, we obtained dynamic maps of the microbubbles flowing in the blood stream, lasting more than one cardiac cycle. After having averaged the volumes with a temporal sliding window of 5 frames, the volumes were exported and dynamic maps were further processed as videos using the Amira 3D software 2021.2 (Thermo Fisher) (e.g. supplementary videos 1 and 2).

2.2.3. Resolution calculation

For analysis, the microbubbles' positions were accumulated to compute a static density map (figures 2(A) and (B)), corresponding to the sum of all the microbubbles detected in each pixel during the whole acquisition. These static maps were used for resolution estimation and vessel segmentation, which was used for the quantitative pulsatility analysis (see below).

The 3D spatial resolution was calculated using the Fourier shell correlation (FSC), also known in 2D as the Fourier ring correlation (FRC), which is a tool used to estimate spatial resolution in single molecule localization microscopy (https://github.com/bionanoimaging/cellSTORM-MATLAB/ (Diederich *et al* 2019)). It was recently introduced to calculate the resolution in ULM in 2D (Hingot *et al* 2021) and in 3D (Heiles *et al* 2022).

Figure 1. 3D DULM pipeline (see methods). SVD: singular value decomposition filtering, PSF: point spread function, MB: microbubbles.

Figure 2. Resolution measurements based on the Fourier shell correlation (FSC). (A) Static density map of the cat brain. (B) Static density map of the mouse brain. (C) FSC calculation. The measured resolutions are 86 μm in the cat brain and 35 μm in the mouse brain.

Figure 3. Pulsatility measurements performed in the 3D volume of the cat brain. (A) Projection of the 3D velocity map of the cat brain, taken at $t = 120$ ms during the acquisition. Two regions of interest (ROI) were selected in the brain. (B) Qualitative velocity variations observed in selected vessels (A1–4) observed in the ROI selected in A, at different time points during the acquisition. (C) Velocity variations over time (600 ms) of vessels A1–4. Vertical lines correspond to the timing of the images displayed in B.

For both species, we randomly separated the tracks across all the buffers into two datasets Im_1 and Im_2, to obtain two independent reconstructions of the same brain volume. After calculating their spectra F_1 and F_2 (corresponding to shells in the Fourier space), we calculated the FSC (figure 2(C)) as the normalized cross-correlation coefficient between F_1 and F_2, along all the voxels r_i located at the radius r:

$$\text{FSC}(r) = \frac{\sum_{r_i \in r} F_1(r_i) \cdot F_2(r_i)^*}{\sqrt{\sum_{r_i \in r}|F_1(r_i)|^2 \cdot \sum_{r_i \in r}|F_2(r_i)|^2}}.$$

The resolution was estimated as the intersection between the FSC curve and the 1/2-bit-threshold curve, as a function of r. This value was compared with the axial and lateral resolutions in diffraction-limited conventional imaging, where the axial resolution is approximately equal to half of the spatial pulse length (i.e. λ in the mouse brain and 2λ in the cat brain) and the lateral resolution LR is given by:
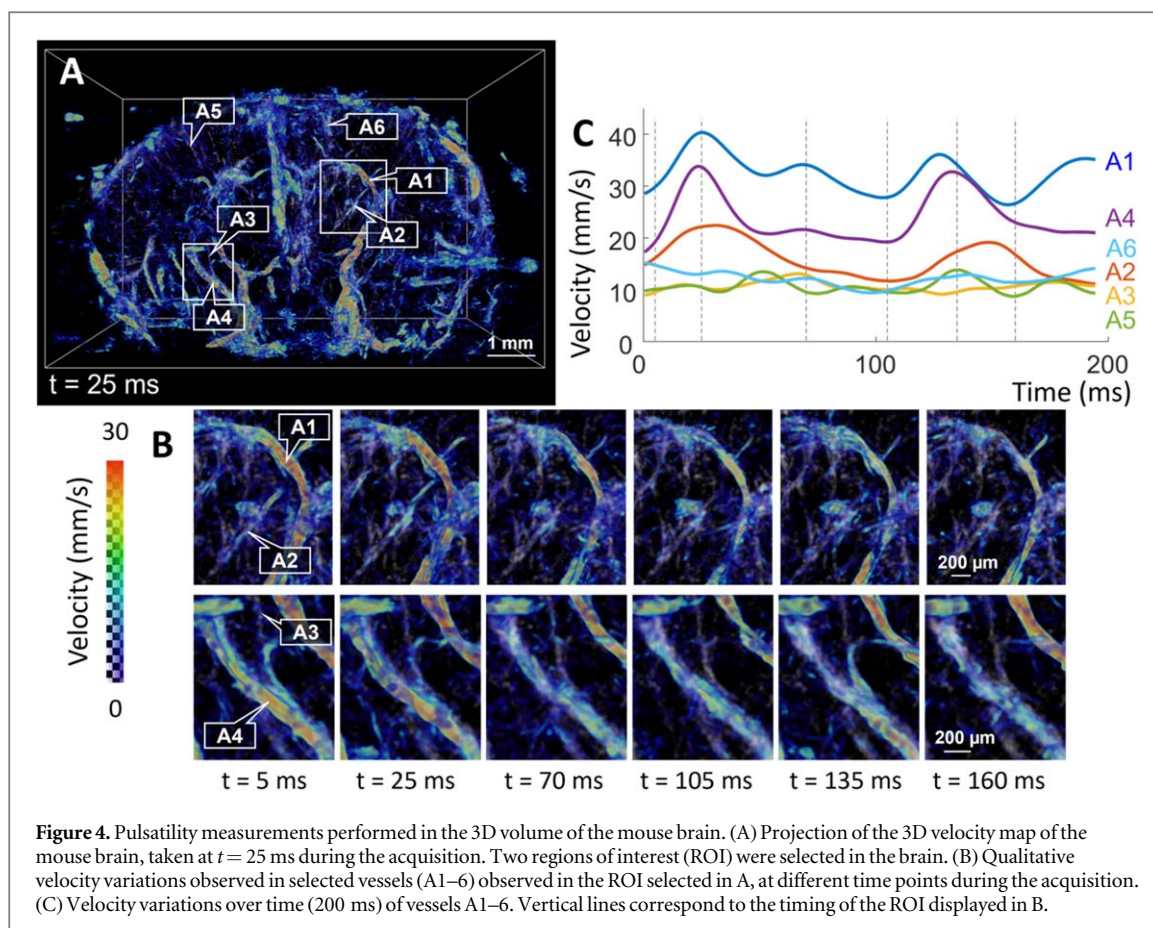
$$LR = \lambda f / d$$

where d is the aperture and f the focal distance (see table 1. Here, the lateral resolution was thus approximately equal to the axial resolution: $\sim 2\lambda$ (i.e. 513 μm at 6 MHz) in the cat brain, and $\sim \lambda$ (i.e. 257 μm at 6 MHz) in the mouse brain.

2.2.4. Segmentation and pulsatility measurements
Vessels were segmented in the static maps using a Hessian filter, with the fibermetric Matlab function based on Frangi's algorithm (Frangi *et al* 1998), with a threshold of 2, 5, 10, 20 and 40 pixels, corresponding to a vessel diameter range of 25–493 μm in the mouse brain and 66–1345 μm in the cat brain. Then, the volumes were binarized. For each vessel, the velocities of all the microbubbles detected within a segmented vessel and within a time interval were averaged. High frequencies in the velocity signal were filtered out (moving average of 100 values in the cat brain, or 75 values in the mouse brain, which corresponds to a frequency cutoff of 10 Hz and 26.67 Hz respectively). The resulting filtered signal was sufficient to sample the cardiac cycles of both species, which had a frequency of 2.67 Hz for the cat and 8.4 Hz for the mouse. Because of this filtering step, the temporal resolution of the velocity variations presented in figures 3(C), 4(C) and 5(B) are 100 ms in the cat brain and 37 ms in the mouse brain.

The pulsatility index (PI) (Gosling and King 1974) was computed as the difference between the peak systolic velocity (PSV) and the end-diastolic velocity (EDV), divided by the mean flow velocity (MFV):

$$PI = \frac{PSV - EDV}{MFV}.$$

Figure 4. Pulsatility measurements performed in the 3D volume of the mouse brain. (A) Projection of the 3D velocity map of the mouse brain, taken at $t = 25$ ms during the acquisition. Two regions of interest (ROI) were selected in the brain. (B) Qualitative velocity variations observed in selected vessels (A1–6) observed in the ROI selected in A, at different time points during the acquisition. (C) Velocity variations over time (200 ms) of vessels A1–6. Vertical lines correspond to the timing of the ROI displayed in B.

2.2.5. Willis circle analysis

In the mouse brain static map (figure 6(A)), the shape of the Willis circle structure could be recognized. This symmetrical structure corresponds to the joining and the branching of several main arteries, in the left and the right hemispheres: the posterior communicating artery (PComA), the internal carotid artery (ICA), the anterior cerebral artery (ACA) and the middle cerebral artery (MCA). Some sections of these arteries were segmented as described above using a Hessian filter, to compute their velocity variations and pulsatility indices.

3. Results

3.1. Resolution calculation

Static density maps obtained after processing can be observed in figures 2(A) and (B).

After calculating the FSC for both species, the resolution in these maps was estimated at 86 μm in the cat brain and 35 μm in the mouse brain (figure 2(C)), which correspond to $\lambda/3$ and $\lambda/7$ respectively ($\lambda \sim 257$ μm at 6 MHz).
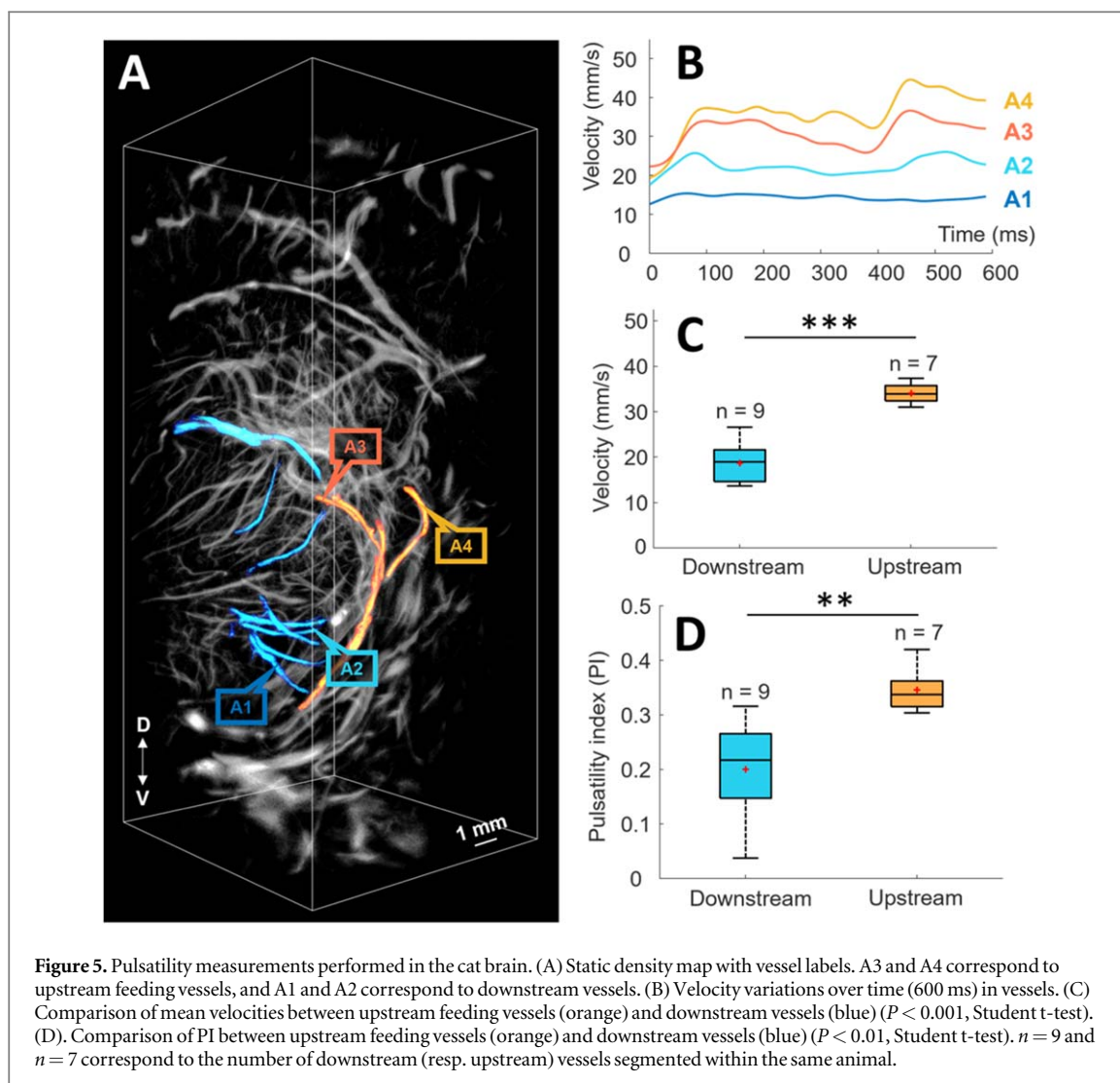
3.2. Qualitative pulsatility measurements

Dynamic maps generated by 3D DULM (supplementary videos 1 and 2) show microbubbles flowing in the bloodstream in the brain in 3D and their velocity variations during the cardiac cycles. The pulsatility can be qualitatively observed in the videos during the cardiac cycles in some large and small vessels shown by the arrows, in both animals.

Figures 3(A) and 4(A) show an example of the 3D velocity map obtained at $t = 120$ ms in the cat brain and $t = 25$ ms in the mouse brain. Two regions of interest (ROI) were extracted from these maps and displayed in figures 3(B) and 4(B) at different time points of the cardiac cycles. Velocity variations could be observed in both large vessels (for example, A1 and A4 in both species), as well as in small vessels (for example, A2 in both species).

3.3. Quantitative pulsatility measurements

A few vessels with different diameters and mean velocities were segmented from these ROI (see Methods), in the cat and the mouse brains, and their velocity variation through time was calculated (figures 3(C) and 4(C)). By doing so, we obtained an overview of the performance of the method applied to different flow patterns: large and

Figure 5. Pulsatility measurements performed in the cat brain. (A) Static density map with vessel labels. A3 and A4 correspond to upstream feeding vessels, and A1 and A2 correspond to downstream vessels. (B) Velocity variations over time (600 ms) in vessels. (C) Comparison of mean velocities between upstream feeding vessels (orange) and downstream vessels (blue) ($P < 0.001$, Student t-test). (D). Comparison of PI between upstream feeding vessels (orange) and downstream vessels (blue) ($P < 0.01$, Student t-test). $n = 9$ and $n = 7$ correspond to the number of downstream (resp. upstream) vessels segmented within the same animal.

small vessels, and fast and slow flow. Blood flow pulsatility was quantified by calculating the PI (Gosling and King 1974) (see methods). Examples of quantitative pulsatility measurements that could be performed in these vessels are shown in tables 2 and 3. The number of microbubble events, i.e. the sum of the microbubbles detected across all the frames, was also given for each vessel.

A reproducible and synchronized pulsatility pattern was observed in both species, even in microvessels with a diameter close to the resolution provided by the FSC calculation (A2: ⌀ 46 μm in the mouse, A2: ⌀ 96 μm in the cat). The velocity variations were coherent with the heart cycle duration of both animals: within the 200 ms cine-loop produced in the mouse brain, we expected to measure 1.7 cardiac cycles (resp. 1.6 cardiac cycles in the cat brain, for a 600 ms cine-loop). Some microvessels also presented a flat velocity variations pattern, with a low PI, such as A3 (⌀ 38 μm, PI: 0.24) in the mouse brain.

In some vessels, the presence of a dicrotic notch was observed, corresponding to a decrease in arterial pressure occurring immediately after the systole. In the cat brain, this dicrotic notch could be observed in vessels A3 and A4, in the mouse brain, it could be observed in vessels A1 and A4.

In the mouse brain, we could also measure different pulsatility indices in some cortical vessels, such as in vessels A5 (PI: 0.42) and A6 (PI: 0.31): A5 has two velocity maxima, whereas A6 presents a flat velocity variations pattern.

3.4. Pulsatility and velocity attenuations along the vascular tree

Large upstream feeding vessels and their subsequent downstream vessels were segmented in the 3D volume of the cat brain (figure 5(A)). Pulsatility measurements were performed in 9 downstream vessels and 7 upstream ones. Examples of the velocity variations in time obtained in these vessels can be observed in figure 5(B).

In figure 5(B), in upstream vessels (A3 and A4), a strong, synchronized, and consistent pulsatility pattern can be observed in the velocity variations. In downstream vessel A2, a smaller but still noticeable pulsatility pattern can be seen. In A1, no pulsatility pattern can be observed.
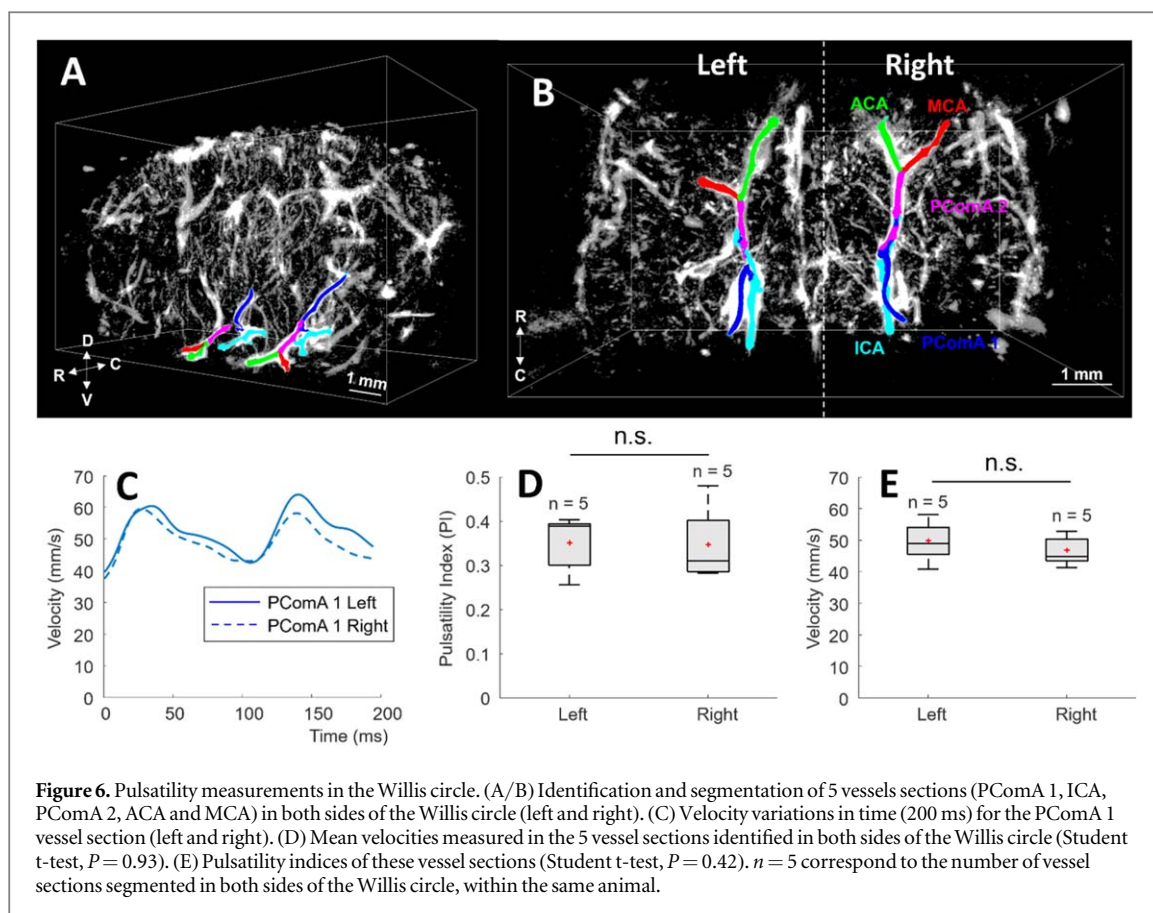
Figure 6. Pulsatility measurements in the Willis circle. (A/B) Identification and segmentation of 5 vessels sections (PComA 1, ICA, PComA 2, ACA and MCA) in both sides of the Willis circle (left and right). (C) Velocity variations in time (200 ms) for the PComA 1 vessel section (left and right). (D) Mean velocities measured in the 5 vessel sections identified in both sides of the Willis circle (Student t-test, $P = 0.93$). (E) Pulsatility indices of these vessel sections (Student t-test, $P = 0.42$). $n = 5$ correspond to the number of vessel sections segmented in both sides of the Willis circle, within the same animal.

Table 2. Examples of Pulsatility Index measurements performed by 3D DULM in the cat brain. MB: microbubbles, PI: pulsatility index.

Vessel	Number of MB events detected	Diameter ⌀ (μm)	Length (mm)	Mean velocity (mm s^{-1})	Pulsatility index
A1	2153 k	212	14	16.81	0.30
A2	734 k	96	16	14.35	0.19
A3	1552 k	154	18	30.80	0.27
A4	1237 k	156	9	25.41	0.37

Table 3. Examples of Pulsatility Index measurements performed by 3D DULM in the mouse brain. MB: microbubbles, PI: pulsatility index.

Vessel	Number of MB events detected	Diameter ⌀ (μm)	Length (mm)	Mean velocity (mm s^{-1})	Pulsatility index
A1	454 k	91	4.2	32.13	0.31
A2	85 k	46	1.7	15.95	0.46
A3	15 k	38	0.9	10.84	0.24
A4	294 k	113	4.1	23.81	0.58
A5	13 k	58	0.4	10.84	0.42
A6	57 k	86	1.0	12.20	0.31

Mean velocity and PI were calculated for each vessel in both groups of vessels (upstream and downstream) in figures 5(C), (D). A significant difference between the two groups, in both, mean velocity ($P < 0.001$) and PI ($P < 0.01$), was observed.

3.5. Intra-animal validation in the Willis circle

Several main arteries belonging to the symmetrical structure of the Willis circle were recognized in the mouse brain and were segmented (figures 6(A), (B)). We found similar velocity waveforms for each vessel between the two sides (left and right) of the Willis circle, with a high pulsatility index and a high velocity, as shown for example in figure 6(I) for the PComA 1 vessel section (represented in dark blue in figures 6(A), (B)).

The pulsatility and mean velocity measurements between the two sides of the brain were compared (figure 6(D)): the PI of all the left vessels was found to be 0.35 ± 0.06, and 0.35 ± 0.08 for the right vessels, the mean velocity was found to be 50 ± 6 mm s^{-1} for the left and 47 ± 5 mm s^{-1} for the right. A Student t-test was performed, and the differences in PI and mean velocity between the left and the right sides of the Willis circle were found to be non-significant (resp. $P = 0.93$ and $P = 0.42$).

4. Discussion

In this study, 3D dynamic ultrasound localization microscopy (3D DULM) was used to image blood velocity as a function of time and to measure pulsatility indices in a cat brain and a mouse brain, with and without craniotomy, respectively. More particularly, DULM could map the cat's brain vasculature down to a few tens of micrometers for the first time.

With 3D DULM, not only highly resolved maps of the brain vasculature were produced (see figure 2), but also cine-loops of flowing microbubbles in the entire volume of the brain, reflecting the blood flow variations during the cardiac cycles. An example of these cine-loops was provided in supplementary videos 1 and 2, in both animals.

This qualitative observation was confirmed with quantitative measurements: in figures 3 and 4, velocity variations over time and PI calculations were extracted for different vessels in the brain, including in large vessels and in cortical ones, and a pulsatile pattern synchronized with the cardiac rhythm of the animals was recognized in the velocity waveforms, even for slow flows and small vessels.

In the cat brain (figure 5), we observed a significant attenuation of the mean velocity and the pulsatility index along the vascular tree, between upstream feeding vessels and downstream subsequent ones. This result is consistent with the cerebral hemodynamics: as the cerebral arteries branch progressively, the resistance increases, leading to a dampening of the pulsatility before it reaches the microcirculation (Vrselja *et al* 2014).

In figure 6, the main arteries in the mouse Willis circle were identified. Their mean velocities and PI were measured and found to be high and reproducible between the left and the right sides of the brain, which is consistent with the literature (Vrselja *et al* 2014, Yankova *et al* 2021).

3D DULM could provide both qualitative and quantitative information on the blood flow pulsatility in the brain, with (1) dynamic 3D maps of microbubbles circulating in the brain, reflecting changes in blood flow during the cardiac cycle; (2) the measurement of velocity variations over time in any observable vessel in the vascular tree, with a <100 ms temporal resolution and a sub-wavelength spatial resolution (<100 μm, i.e. λ/2.5), and (3) the PI estimation in these vessels, to quantify the pulsatility. Until now, in small animals, the pulsatility could only be quantified using TCD or MRI in the carotid (Hartley *et al* 2011), in the Willis circle (Bonnin *et al* 2008, Li *et al* 2010, Cahill *et al* 2014, Wei *et al* 2019, Lebas *et al* 2023), in small vessels at the surface of the brain (Baraghis *et al* 2011, Santisakultarm *et al* 2012), or in a 2D section of the brain using 2D DULM (Bourquin *et al* 2021), or more recently in 2D ULM with the help of a deep-learning technique (Chen *et al* 2023). With 3D DULM, we were able to extract pulsatility measurements in a large range of vessels along the cerebral vascular tree, in depth, in 3D, with a high spatiotemporal resolution. With this technique, dynamic measurements could be extracted in a range of vessels that were inaccessible for brain imaging modalities before. Such a modality could be used for example to study the pulsatility propagation in the brain vasculature and to better understand its impact on microvessels. This technique could also be used in other organs such as the kidney, where dynamic blood flow parameters such as the pulsatility are also important metrics to monitor (Heine *et al* 2005, Madero *et al* 2013).

The study presented herein is however not without limitations.

This study has been performed on two species, but only in one animal each (one cat and one mouse). It is a proof-of-concept that one can measure the pulsatility in the vascular tree using 3D DULM, but a study on a larger number of animals would be necessary to validate its reproducibility, especially since the Willis circle anatomy may vary from one animal to another (Qian *et al* 2018).

To our knowledge, no *in vivo* pulsatility measurements were performed deep in the brain in the cat brain before, which make them difficult to compare with the literature. In the rodent brain, some studies were done in the Willis circle, e.g. in fetal mice brains using ultrasound biomicroscopy (UBM) (Cahill *et al* 2014) and in mice and rat brains using TCD (Bonnin *et al* 2008, Li *et al* 2010, Lebas *et al* 2023) or MRI (Wei *et al* 2019). In adult mice studies, the measurements or simulations performed by different methods show a large range of maximal, minimal and mean velocity values in the Willis circle arteries, between ~50 and 200 mm s^{-1}. The values we obtained in the Willis circle are on the lower end of that range (50 ± 6 mm s^{-1} for the left and 47 ± 5 mm s^{-1} for the right hemisphere). Another study in 3D ULM reported for example a maximal velocity of 64 mm s^{-1} in the rat brain (McCall *et al* 2023), while studies in TCD this animal model show peak systolic velocities up to 81.6 cm s^{-1} (Li *et al* 2010). This bias may be due to the fact that tracking algorithms tend to favor local pairing:

fast microbubbles move far from one frame to the next, leading to ambiguity in the optimal pairing. Future work should be done to better understand ULM and DULM limitations in terms of hemodynamic quantification.

This study was conducted using experimental procedures primarily designed to study the functional activity of the visual cortex, which rely on urethane as an anesthetic. Indeed, other anesthetics such as isoflurane can induce large modifications in the blood flow due to their vasodilating effects (Sullender *et al* 2022), whereas urethane is known to have a smaller impact (Shumkova *et al* 2021). But urethane is lethal, so it cannot be used in experiments where animals are followed for several days, weeks or months. The experiments were also invasive for both animals (craniotomy in the cat and skin removal in the mouse) and were done after a 3 d optical procedure on the cat, which may have affected the pulsatility measurements compared to what could have been done non-invasively on awaken animals.

Our experimental set up relied on an initial bolus injection, which leads to a variation in the microbubble concentration over time during the acquisition. Although bolus injection is a frequently used method in ULM, a continuous infusion could have been used (Christensen-Jeffries *et al* 2020), which may be optimized to improve resolution and decrease the acquisition time by better controlling microbubble concentrations (Belgharbi *et al* 2023).

For now, DULM relies on the triggering of the ultrasound sequence on the ECG to start each group of frames acquired with an R-wave of the ECG and thus ensure the synchronicity between the groups. But in Wiersma *et al* (2022), another group showed in silico that pulsatility could be retrieved in the microbubbles tracks without ECG-gating. Also, it could be possible to measure, in each group, the microbubbles density in a large vessel as in Yu *et al* (2018) or the tissue movement to temporally register the images according to their timing in the cardiac cycles. ECG-gating would thus not be mandatory to perform DULM: one could extract dynamic measurements from a regular ULM sequence. This is an ongoing study in our group.

The maximal frame rate we could achieve was limited by multiplexing: indeed, we used a fully addressed probe driven by only one ultrasound scanner, so each frame required to perform four Transmits/Receives per angle. A combination of several ultrasound systems, such as the one described in Demeulenaere *et al* (2022b), may overcome such a limitation and allow for performing several angles while keeping a high frame rate and a large penetration depth, but at a much higher cost.

The ~15 min sequences also included pauses for the transfer and the saving of the data. This may be an issue for the pulsatility estimation since our measurement relies on the averaging of groups of frames acquired during the whole acquisition, and the blood flow velocity may fluctuate in the meantime. However, as it is mentioned in Heiles *et al* (2019), this drawback of performing volumetric images will decrease in the coming years with the increase of transfer speed and computational power: For example, without the pauses in the sequence, the mouse brain could have been imaged with a 3 min acquisition, dividing the acquisition time five-fold.

The achieved temporal resolution of ~0.1 s in this study was not sufficient to measure an increase in the time of arrival of the pulsatile flow along the vascular tree, but this could be another interesting biomarker to measure in the study of neurodegenerative diseases.

Also, the temporal length of a group (600 ms in the cat brain and 200 ms in the mouse brain) allowed us to measure fewer than two cardiac cycles in each animal (1.6 cardiac cycles in the cat and 1.7 cardiac cycles in the mouse). Thus, the reproducibility of the measurement could not be validated between two consecutive cardiac cycles—such a validation was however performed by our group in a previous study in 2D DULM, in the rat and the mouse brains (Bourquin *et al* 2021).

In the current study, animals were placed in a stereotaxic frame, resulting in negligible motion and breathing artifacts. Through initial analysis, we determined that motion correction had minimal influence on pulsatility measurements in segmented vessels. However, future studies will characterize pulsatility measurements in the context of motion and aberration correction (Demené *et al* 2021, Xing *et al* 2023).

In the pipeline we used to process the data, several thresholds were set empirically (filter coefficients, Hessian filter parameters, correlation thresholds, etc), that may differ from one animal to the other, or even from one dataset to another. This is a limitation of this study: variations in the thresholds may have consequences in the measured pulsatility. Further calibration studies against a gold-standard are needed.

Moreover, the sub-wavelength spatial resolutions we obtained (86 μm in the cat brain and 35 μm in the mouse brain, corresponding to $\lambda/3$ and $\lambda/7$ respectively) are not as small as the ones reported in previous 3D ULM studies. For example, two non-invasive studies in the rat brain (Chavignon *et al* 2022a, McCall *et al* 2023) and one through the skull without the skin in the mouse brain (Demeulenaere *et al* 2022a) reported a spatial resolution of 31 μm, 31 μm and 20 μm respectively. This can be explained by different factors. First, this study was performed using a single ultrasound scanner, and only one angle (at 0°) was used in the sequences to maintain a high frame rate despite the limited transfer rate of the host computer used at the time of this study. Hence, the quality of the images and the resolution could have been improved by using several compounding angles, in the lateral and the elevation directions, or even by exploring other multiplexing combinations such as the 'light' sequence described in Chavignon *et al* (2022a). Moreover, the probe we used is known to have

misaligned panels as it was also pointed out in Chavignon *et al* (2022a), which can lead to artifacts in the near-field—especially in the mouse brain. A small tank of water could have been added to offset the surface of the probe as it is done in Demeulenaere *et al* (2022a) and thus limiting these artifacts in the near-field. Better contrast was achieved in the cat brain; one can speculate that using a 6 MHz pulse in the mouse brain is more subject to clutter due to its small size, e.g. from multiple reflections on the skull. DULM relies on high microbubble concentrations to increase the number of detections in comparison to ULM. Simulations (Belgharbi *et al* 2023) indicate that an optimal concentration exists, but it is difficult to achieve this optimal value experimentally because of the variability linked to microbubble destruction at the injection site, and the bolus injection dynamics. Infusions could also be used, but are also associated with experimental challenges, especially in small animals, in which injected fluid volumes are limited.

However, compared to the diffraction-limited axial and lateral resolutions that can be obtained (see Methods) with the matrix probe that we used, at 6 MHz, the resolution that we achieved shows a gain of a factor $\sim$6 in the cat brain and a gain of a factor $\sim$7 in the mouse brain. These resolutions are comparable with the ones obtained with a similar probe (at 7.8 MHz) and a similar sequence in Lok *et al* (2022), which achieved a 52 μm resolution at an 11 mm depth in a chicken embryo brain, corresponding to a gain of a factor $\sim$ 4, in both lateral and axial directions.

5. Conclusion

3D DULM is a novel ultrasound imaging technique that generates dynamic maps of flowing microbubbles in the vasculature in the brain, and performs quantitative pulsatility measurements. This approach can be used to obtain dynamic information along the cerebral vascular tree, in both large feeding vessels and microvessels, in-depth and in 3D. Such a technology could be used as an adjunct biomarker in the study of neurodegenerative diseases.

Acknowledgments

Data availability statement

The data cannot be made publicly available upon publication because the cost of preparing, depositing and hosting the data would be prohibitive within the terms of this research project. The data that support the findings of this study are available upon reasonable request from the authors.

ORCID iDs

Chloé Bourquin https://orcid.org/0000-0002-1360-0692
Jonathan Porée https://orcid.org/0000-0002-4179-9264
Brice Rauby https://orcid.org/0000-0003-0737-7954
Vincent Perrot https://orcid.org/0000-0002-0940-5667
Nin Ghigo https://orcid.org/0000-0001-6526-5868
Hatim Belgharbi https://orcid.org/0000-0001-9534-1796
Gerardo Ramos-Palacios https://orcid.org/0000-0003-0861-6152
Nelson Cortes https://orcid.org/0000-0001-5469-910X
Hugo Ladret https://orcid.org/0000-0001-7999-3751

Lamyae Ikan ⓘ https://orcid.org/0009-0008-4114-1965
Christian Casanova ⓘ https://orcid.org/0000-0002-1494-8391
Frédéric Lesage ⓘ https://orcid.org/0000-0003-3699-1283
Jean Provost ⓘ https://orcid.org/0000-0003-2057-2199

References

Baraghis E, Bolduc V, Lefebvre J, Srinivasan V J, Boudoux C, Thorin E and Lesage F 2011 Measurement of cerebral microvascular compliance in a model of atherosclerosis with optical coherence tomography *Biomed. Opt. Express, BOE* **2** 3079–93

Belgharbi H, Porée J, Damseh R, Perrot V, Milecki L, Delafontaine-Martel P, Lesage F and Provost J 2023 An anatomically realistic simulation framework for 3D ultrasound localization microscopy *IEEE Open J. Ultrason., Ferroelectrics, Freq. Control* **3** 1–13

Berthon B, Morichau-Beauchant P, Porée J, Garofalakis A, Tavitian B, Tanter M and Provost J 2018 Spatiotemporal matrix image formation for programmable ultrasound scanners *Phys. Med. Biol.* **63** 03NT03

Bonnin P, Debbabi H, Mariani J, Charriaut-Marlangue C and Renolleau S 2008 Ultrasonic assessment of cerebral blood flow changes during ischemia-reperfusion in 7 d old rats *Ultrasound Med. Biol.* **34** 913–22

Bourquin C, Porée J, Lesage F and Provost J 2022 *In vivo* pulsatility measurement of cerebral microcirculation in rodents using dynamic ultrasound localization microscopy *IEEE Trans. Med. Imaging* **41** 782–92

Cahill L, Zhou Y-Q, Seed M, Macgowan C and Sled J 2014 Brain sparing in fetal mice: BOLD MRI and doppler ultrasound show blood redistribution during hypoxia *J. Cereb. Blood Flow Metab.* **34** 1082–8

Chavignon A, Heiles B, Hingot V, Orset C, Vivien D and Couture O 2022a 3D transcranial ultrasound localization microscopy in the rat brain with a multiplexed matrix probe *IEEE Trans. Biomed. Eng.* **69** 2132–42

Chavignon A, Hingot V, Orset C, Vivien D and Couture O 2022b 3D transcranial ultrasound localization microscopy for discrimination between ischemic and hemorrhagic stroke in early phase *Sci. Rep.* **12** 14607

Chen X, Lowerison M R, Dong Z, Chandra Sekaran N V, Llano D A and Song P 2023 Localization free super-resolution microbubble velocimetry using a long short-term memory neural network *IEEE Trans. Med. Imaging* **42** 2374–85

Christensen-Jeffries K *et al* 2020 Super-resolution ultrasound imaging *Ultrasound Med. Biol.* **46** 865–91

Christensen-Jeffries K, Browning R J, Tang M-X, Dunsby C and Eckersley R J 2015 *In vivo* acoustic super-resolution and super-resolved velocity mapping using microbubbles *IEEE Trans. Med. Imaging* **34** 433–40

Chung C-P, Lee H-Y, Lin P-C and Wang P-N 2017 Cerebral artery pulsatility is associated with cognitive impairment and predicts dementia in individuals with subjective memory decline or mild cognitive impairment *J. Alzheimers Dis.* **60** 625–32

Cormier P, Porée J, Bourquin C and Provost J 2021 Dynamic myocardial ultrasound localization angiography *IEEE Trans. Med. Imaging* **40** 3379–88

Cortes N, Demers M, Ady V, Ikan L and Casanova C 2022 Reliable, fast and stable contrast response function estimation *Vision* **6** 62

Couture O, Besson B, Montaldo G, Fink M and Tanter M 2011 Microbubble ultrasound super-localization imaging (MUSLI) *IEEE Int. Ultrasonics Symp. (Orlando, FL, USA)* pp 1285–7

Couture O, Hingot V, Heiles B, Muleki Seya P and Tanter M 2018 Ultrasound localization microscopy and super-resolution: a state of the art *IEEE Trans. Ultrason. Ferroelectr. Freq. Control* **65** 1304–20

Demené C, Robin J, Dizeux A, Heiles B, Pernot M, Tanter M and Perren F 2021 Transcranial ultrafast ultrasound localization microscopy of brain vasculature in patients *Nat. Biomed. Eng.* **5** 219–28

Demeulenaere O *et al* 2022b Coronary flow assessment using 3-dimensional ultrafast ultrasound localization microscopy *JACC: Cardiovascular Imaging* **15** 1193–208

Demeulenaere O, Bertolo A, Pezet S, Ialy-Radio N, Osmanski B, Papadacci C, Tanter M, Deffieux T and Pernot M 2022a *In vivo* whole brain microvascular imaging in mice using transcranial 3D ultrasound localization microscopy *eBioMedicine* **79** 103995

Denis L *et al* 2023 Sensing ultrasound localization microscopy for the visualization of glomeruli in living rats and humans *eBioMedicine* **91** 104578

Diederich B, Then P, Jügler A, Förster R and Heintzmann R 2019 Cellstorm-cost-effective super-resolution on a cellphone using dSTORM *PLoS One* **14** e0209827

Errico C, Pierre J, Pezet S, Desailly Y, Lenkei Z, Couture O and Tanter M 2015 Ultrafast ultrasound localization microscopy for deep super-resolution vascular imaging *Nature* **527** 499–502

Foiret J, Zhang H, Ilovitsh T, Mahakian L, Tam S and Ferrara K W 2017 Ultrasound localization microscopy to image and assess microvasculature in a rat kidney *Sci. Rep.* **7** 13662

Frangi A F, Niessen W J, Vincken K L and Viergever M A 1998 *Multiscale Vessel Enhancement Filtering Medical Image Computing and Computer-Assisted Intervention — MICCAI'98 Lecture Notes in Computer Science* ed W M Wells *et al* (Springer) pp 130–7

Gosling R G and King D H 1974 Arterial assessment by doppler-shift ultrasound *Proc. R. Soc. Med.* **67** 447–9

Guo H 2011 A simple algorithm for fitting a gaussian function [DSP tips and tricks] *IEEE Signal Process. Mag.* **28** (5) 134–7

Hartley C J, Reddy A K, Madala S, Entman M L, Michael L H and Taffet G E 2011 Doppler velocity measurements from large and small arteries of mice *Am. J. Physiol.-Heart and Circ. Physiol.* **301** H269–78

Heiles B, Chavignon A, Bergel A, Hingot V, Serroune H, Maresca D, Pezet S, Pernot M, Tanter M and Couture O 2022 Volumetric ultrasound localization microscopy of the whole rat brain microvasculature *IEEE Open J. Ultrasonics, Ferroelectrics, Freq. Control* **2** 261–82

Heiles B, Correia M, Hingot V, Pernot M, Provost J, Tanter M and Couture O 2019 Ultrafast 3D ultrasound localization microscopy using a 32 × 32 matrix array *IEEE Trans. Med. Imaging* **38** 2005–15

Heine G H, Gerhart M K, Ulrich C, Kaler H and Girndt M 2005 Renal doppler resistance indices are associated with systemic atherosclerosis in kidney transplant recipients *Kidney Int.* **68** 878–85

Hingot V *et al* 2020 Early ultrafast ultrasound imaging of cerebral perfusion correlates with ischemic stroke outcomes and responses to treatment in mice *Theranostics* **10** 7480–91

Hingot V, Chavignon A, Heiles B and Couture O 2021 Measuring image resolution in ultrasound localization microscopy *IEEE Trans. Med. Imaging* **40** 3812–9

Huang C *et al* 2021 Super-resolution ultrasound localization microscopy based on a high frame-rate clinical ultrasound scanner: an in-human feasibility study *Phys. Med. Biol.* **66** 08NT01

Lebas H, Boutigny A, Maupu C, Salfati J, Orset C, Mazighi M, Bonnin P and Boulaftali Y 2023 Imaging cerebral arteries tortuosity and velocities by transcranial doppler ultrasound is a reliable assessment of brain aneurysm in mouse models *Stroke: Vascular Interventional Neurol.* **3** e000476

Li L, Ke Z, Tong K Y and Ying M 2010 Evaluation of cerebral blood flow changes in focal cerebral ischemia rats by using transcranial doppler ultrasonography *Ultrasound Med. Biol.* **36** 595–603

Lok U-W, Huang C, Trzasko J D, Kim Y, Lucien F, Tang S, Gong P, Song P and Chen S 2022 Three-dimensional ultrasound localization microscopy with bipartite graph-based microbubble pairing and kalman-filtering-based tracking on a 256-channel verasonics ultrasound system with a 32 × 32 Matrix array *J. Med. Biol. Eng.* **42** 767–79

Lowerison M R, Sekaran N V C, Zhang W, Dong Z, Chen X, Llano D A and Song P 2022 Aging-related cerebral microvascular changes visualized using ultrasound localization microscopy in the living mouse *Sci. Rep.* **12** 619

Madero M *et al* (Study for the H A) 2013 Association of arterial rigidity with incident kidney disease and kidney function decline: the health ABC study *Clin. J. Am. Soc. Nephrol.* **8** 424

McCall J R, Santibanez F, Belgharbi H, Pinton G F and Dayton P A 2023 Non-invasive transcranial volumetric ultrasound localization microscopy of the rat brain with continuous, high volume-rate acquisition *Theranostics* **13** 1235–46

Moldestad O, Karlsen P, Molden S and Storm J F 2009 Tracheotomy improves experiment success rate in mice during urethane anesthesia and stereotaxic surgery *J. Neurosci. Methods* **176** 57–62

Perrot V, Polichetti M, Varray F and Garcia D 2021 So you think you can DAS? a viewpoint on delay-and-sum beamforming *Ultrasonics* **111** 106309

Qian B, Rudy R F, Cai T and Du R 2018 Cerebral artery diameter in inbred mice varies as a function of strain *Front. Neuroanat.* **12** 10

Renaudin N, Demené C, Dizeux A, Ialy-Radio N, Pezet S and Tanter M 2022 Functional ultrasound localization microscopy reveals brain-wide neurovascular activity on a microscopic scale *Nat. Methods* **19** 1004–12

Roher A E *et al* 2011 Transcranial doppler ultrasound blood flow velocity and pulsatility index as systemic indicators for Alzheimer's disease *Alzheimers Dement* **7** 445–55

Santisakultarm T P, Cornelius N R, Nishimura N, Schafer A I, Silver R T, Doerschuk P C, Olbricht W L and Schaffer C B 2012 *In vivo* two-photon excited fluorescence microscopy reveals cardiac- and respiration-dependent pulsatile blood flow in cortical blood vessels in mice *Am. J. Physiol.-Heart Circ. Physiol.* **302** H1367–77

Shahriari S and Garcia D 2018 Meshfree simulations of ultrasound vector flow imaging using smoothed particle hydrodynamics *Phys. Med. Biol.* **63** 205011

Shumkova V, Sitdikova V, Rechapov I, Leukhin A and Minlebaev M 2021 Effects of urethane and isoflurane on the sensory evoked response and local blood flow in the early postnatal rat somatosensory cortex *Sci Rep.* **11** 9567

Stutzman W L and Thiele G A 2012 *Antenna Theory and Design* (Wiley)

Sullender C T, Richards L M, He F, Luan L and Dunn A K 2022 Dynamics of isoflurane-induced vasodilation and blood flow of cerebral vasculature revealed by multi-exposure speckle imaging *J. Neurosci. Methods* **366** 109434

Taghavi I, Andersen S B, Hoyos C A V, Schou M, Gran F, Hansen K L, Nielsen M B, Sørensen C M, Stuart M B and Jensen J A 2022 Ultrasound super-resolution imaging with a hierarchical Kalman tracker *Ultrasonics* **122** 106695

Tang S, Song P, Trzasko J D, Lowerison M, Huang C, Gong P, Lok U-W, Manduca A and Chen S 2020 Kalman filter-based microbubble tracking for robust super-resolution ultrasound microvessel imaging *IEEE Trans. Ultrason. Ferroelectr. Freq. Control* **67** 1738–51

Tomek A, Urbanová B and Hort J 2014 Utility of transcranial ultrasound in predicting Alzheimer's disease risk *J. Alzheimers Dis.* **42** S365–74

Van den Kerkhof M, van der Thiel M M, van Oostenbrugge R J, Postma A A, Kroon A A, Backes W H and Jansen J F 2023 Impaired damping of cerebral blood flow velocity pulsatility is associated with the number of perivascular spaces as measured with 7T MRI *J. Cereb. Blood Flow Metab.* **43** 937–46

Vrselja Z, Brkic H, Mrdenovic S, Radic R and Curic G 2014 Function of circle of Willis *J. Cereb. Blood Flow Metab.* **34** 578–84

Wei Z, Chen L, Lin Z, Jiang D, Xu J, Liu P, van Zijl P C M and Lu H 2019 Optimization of phase-contrast MRI for the estimation of global cerebral blood flow of mice at 11.7T *Magn. Reson. Med.* **81** 2566–75

Wiersma M, Heiles B, Kalisvaart D, Maresca D and Smith C S 2022 Retrieving pulsatility in ultrasound localization microscopy *IEEE Open J. Ultrasonics, Ferroelectrics, Freq. Control* **2** 283–98

Xing P, Porée J, Rauby B, Malescot A, Martineau É, Perrot V, Rungta R L and Provost J 2023 Phase aberration correction for in vivo ultrasound localization microscopy using a spatiotemporal complex-valued neural network *IEEE Transactions on Medical Imaging* **43** 662–73

Xu X, Sun L, Cannata J M, Yen J T and Shung K K 2008 High-frequency ultrasound doppler system for biomedical applications with a 30 MHz linear array *Ultrasound Med. Biol.* **34** 638–46

Yan J *et al* 2023 Transthoracic super-resolution ultrasound localisation microscopy of myocardial vasculature in patients arXiv:2303.14003

Yankova G, Tur D, Parshin D, Cherevko A and Akulov A 2021 Cerebral arterial architectonics and CFD simulation in mice with type 1 diabetes mellitus of different duration *Sci. Rep.* **11** 3969

Yu J, Lavery L and Kim K 2018 Super-resolution ultrasound imaging method for microvasculature *in vivo* with a high temporal accuracy *Sci. Rep.* **8** 13918